Supplementary Information
Spin Dependent Tunneling and Strain Sensitivity in Co_2MnSb/HfIrSb Magnetic Tunneling Junction: A First-Principles Study

Joydipto Bhattacharya[1,2], Ashima Rawat[3], Ranjit Pati[3], Aparna Chakrabarti[†1,2], Ravindra Pandey[3]
[1]*Raja Ramanna Centre for Advanced Technology, Indore 452013, India*
[2]*Homi Bhabha National Institute, Training School Complex, Anushakti Nagar, Mumbai 400094, India and*
[3]*Department of Physics, Michigan Technological University, Houghton, Michigan 49931, USA*

I. GEOMETRIC & ELECTRONIC PROPERTIES OF BULK

Table 1 summarizes the calculated physical properties of the bulk electrode material Co_2MnSb. Consistent with the Slater-Pauling formula, Co_2MnSb exhibits HM behavior with a total magnetic moment of 6 μ_B per formula unit and a predicted high Curie temperature. DFT calculations demonstrate that the HM character is defect tolerant, making it an attractive candidate for spin-injecting devices. However, some disordered states have been found to exceed the predicted magnetic moment, suggesting a possible higher Curie temperature than the parent compound. The spin-resolved band structure (Figure S1) confirms the HM behavior with a gap of 0.42 eV in the minority spin channel. The symmetry of the bands crossing the Fermi energy (E_F) is also important to understand, and from the symmetry analyses, it is confirmed that in the majority spin channel, the lower energy band crossing the E_F possesses a Δ_1 symmetry, while the doubly degenerate higher energy bands correspond to the Δ_5 symmetry. This orbital symmetry character is similar to that of Co_2MnSi alloy[1], which has been extensively studied as an electrode material for MTJ systems. The significance of the presence of bands with Δ_1 symmetry will be discussed later.

Understanding how bi-axial strain affects the electronic and magnetic properties of electrode materials is crucial, particularly in investigating the heterostructure properties where strain can arise from the substrate or metal-insulator interfaces. In this study, we considered both compression and expansion of the in-plane lattice parameters (a and b), and the geometry was not allowed to relax. The in-plane strain with respect to the undistorted structure is summarized in Table S3, and the spin-polarized DOS with compressive and tensile strain is shown in Figure S2. We observed that the HM property is maintained over the entire range of tensile strain, and the center of the HM gap shifts towards the conduction band, such that the position of the Fermi level (E_F) lies within the gap. However, compressive bi-axial strain appeared to destroy the HM property, as it caused the minority spin states to shift towards E_F, thereby reducing both the spin polarization value at E_F and the magnetic moment (Table S3).

We further investigated the effect of bi-axial strain on the majority and minority spin band structure along the Γ to X direction (i.e., along the propagation direction) in Figures S3, S4, and S5. Rigid shift of the bands with no significant impact on the band dispersion has been observed. Given that Co_2MnSb loses its HM properties under compressive bi-axial strain, we examine the orbital character of the bands near E_F in the minority spin channel. In Figure S3, we present the contribution of the Δ_1 orbitals to the minority spin bands under compressive bi-axial strain. We observe that the bands crossing at E_F have a dominant Δ_1 character, which is likely to contribute to the electron transmission across the junction. This could significantly affect the TMR value, as we will discuss later in this paper.
In Figure. S6, the band structure of HfIrSb with SOC is presented. The introduction of SOC breaks the degeneracy of the valence bands at the Γ point, leading to a reduction of the band gap to 0.67 eV. Furthermore, we observe the splitting of valence bands as we move away from Γ. Notably, conduction bands near the Γ point exhibits a Zeeman-like spin splitting of bands. Analyzing the orbital-projected bands (Figure.S6 (b) - (d)) incorporating SOC, we discern that while the CBM is predominantly of Δ_1 orbital character, the valence band maximum (VBM) is primarily characterized by the Δ_5 orbital

II. ELECTRONIC PROPERTIES COMPARISON USING VASP AND QE

In Fig. S7, the electronic structure of bulk Co_2MnSb and HfIrSb is illustrated, as calculated by two distinct software platforms, VASP[7] and QE[8]. Notably, the electronic properties derived from these two plane-wave based programs exhibit remarkable consistency. Nevertheless, a nuanced distinction emerges in the half-metallic gap values, with VASP indicating a gap of approximately 0.42 eV, while QE yields a slightly higher value of 0.49 eV. Similarly, the band gap of HfIrSb exhibits subtle variations, with VASP predicting a gap of 0.87 eV and QE indicating a marginally lower value of 0.84 eV.

III. ELECTRONIC AND MAGNETIC PROPERTIES OF SURFACE

The performance of spintronic devices heavily relies on the surface properties of electrode materials. In

Table S1. Calculated bulk properties of the relevant full and half Heusler alloys: equilibrium lattice parameter a in Å, band gap energy from the Fermi level E_g (HM written in brackets indicates that the material is half-metallic) in eV, Spin magnetic moment M_S given in μ_B per f.u. In the last column, we report the symmetries of the bands that cross the E_F of the electrode and the symmetries associated to the valence band maxima (VBM) and conduction band minima (CBM) of the spacer materials, respectively. Values from the literature are given inside brackets, with the references mentioned in the superscript.

Material	a	E_g	M_S	Role	Band Symmetry
					VBM, CBM
Co_2MnSb	6.01 (Expt. 5.96[2])	0.42(HM)(0.49(HM)[3])	6.00 (6.00[a])	Electrode	Δ_5, Δ_1
HfIrSb	6.33 (Expt. 6.34[4])	0.87 (0.89)[5,6] (Expt.1.3[4])	0	Spacer	Δ_2, Δ_5 & Δ_1

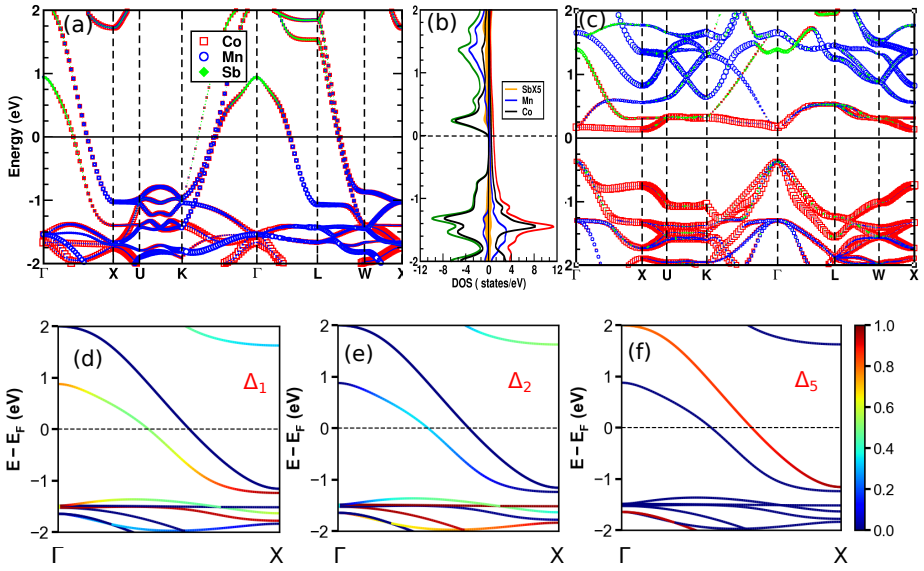

Figure S1. Panels (a), (c) show the majority and minority spin band structure, (b) depicts spin-polarized DOS of the bulk Co2MnSb structure. Panels (d), (e), and (f) display the orbital projected majority spin band structure along the Γ to X (Z) direction, where Δ_1, Δ_2, and Δ_5 represent the (s, p_z, d_{z^2}), (d_{xy}, $d_{x^2-y^2}$), and (p_x, p_y, d_{xz}, d_{yz}) orbital characters, respectively.

Table S2. In plane strain, total and atomic magnetic moment (μ_T & μ_{Co}, μ_{Mn}) and spin polarization (in %) at E_F, calculated for the Co_2MnSb bulk structure.

In-plane strain (%)	c/a ratio	Magnetic moment (in μ_B)			Spin-polarization (in %)
		μ_T	μ_{Co}	μ_{Mn}	
-5	1.05	5.28	1	3.27	-46
-4	1.04	5.56	1.10	3.33	-52
-3	1.03	5.70	1.16	3.38	-32
-2	1.02	5.84	1.21	3.42	-31
-1	1.01	5.93	1.24	3.45	50
1	0.99	5.99	1.24	3.49	100
2	0.98	6.00	1.23	3.50	100
3	0.97	5.99	1.23	3.52	100
4	0.96	6.00	1.23	3.54	100
5	0.95	6.00	1.23	3.55	100

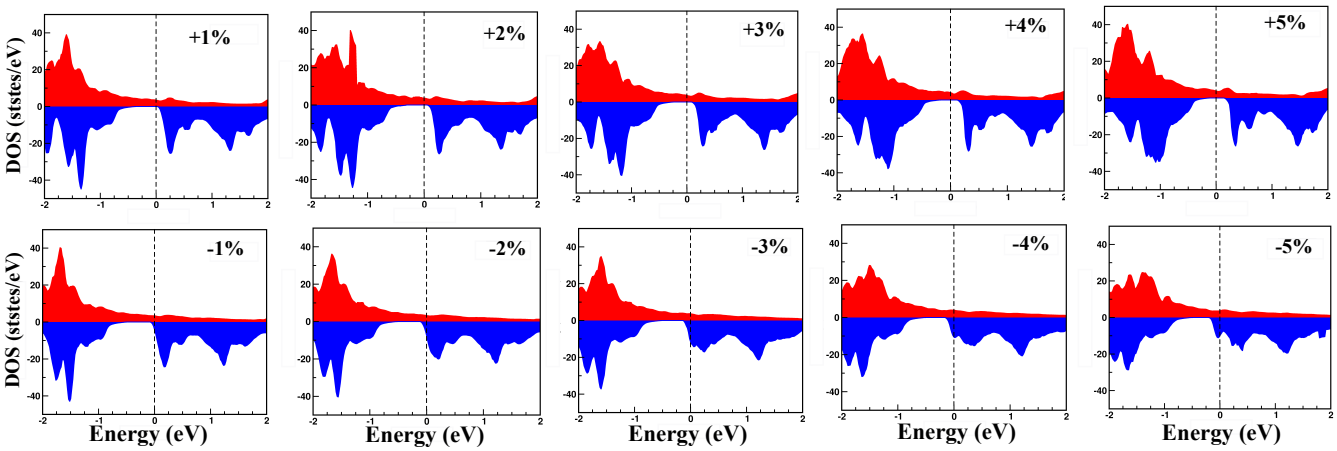

Figure S2. DOS of bulk Co_2MnSb under biaxial strain ($\pm 5\%$) shown in two panels. The top panel corresponds to tensile strain, while the bottom panel corresponds to compressive strain.Here, red (blue) represent majority (minority) spin states.

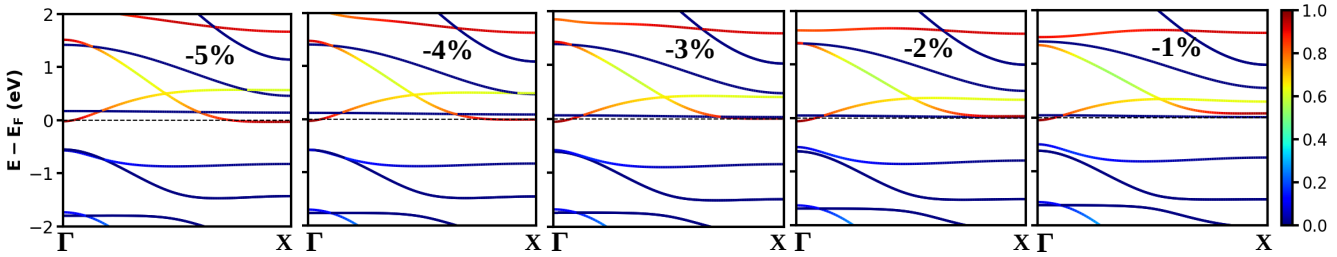

Figure S3. Effect of compressive bi-axial strain on the minority spin bands of the bulk Co_2MnSb. Here we have only shown the contribution from the Δ_1 orbitals.

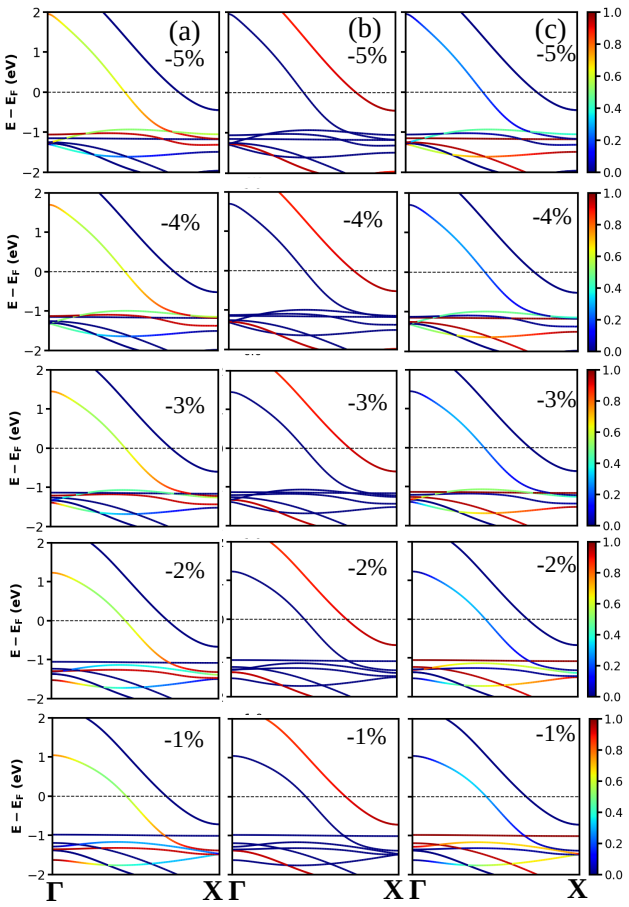

Figure S4. The majority spin band structure of bulk Co_2MnSb under compressive biaxial strain (-1 to -5 %) is shown, where panels (a), (b), and (c) depict the orbital-projected majority spin band structure along the Γ to X (Z) direction. Here Δ_1 (a), Δ_5 (b), and Δ_2 (c) represent the (s, p_z, d_{z^2}), (p_x, p_y, d_{xz}, d_{yz}), and (d_{xy}, $d_{x^2-y^2}$) orbital characters, respectively.

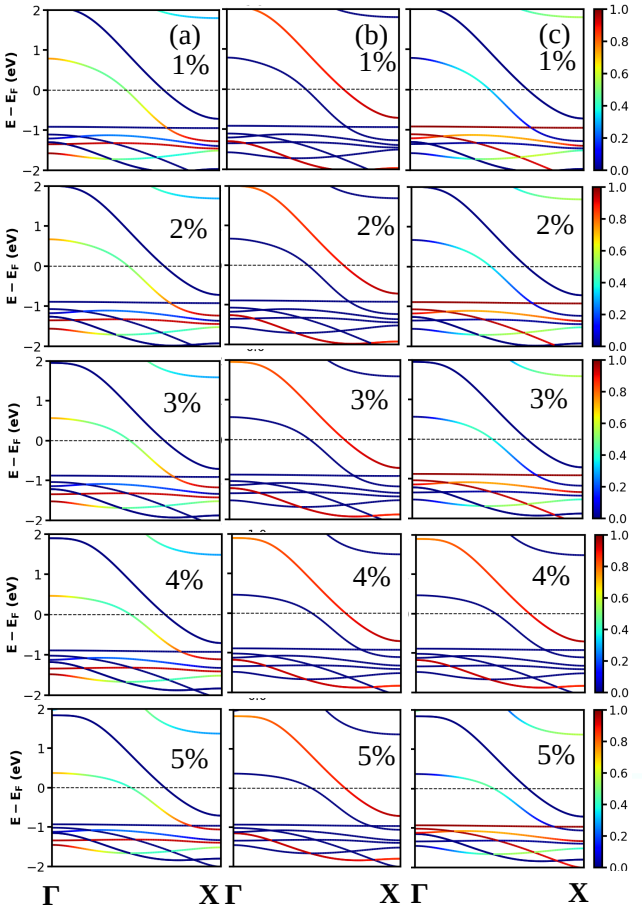

Figure S5. The majority spin band structure of bulk Co2MnSb under tensile bi-axial strain (1 to 5 %) is shown, where panels (a), (b), and (c) depict the orbital-projected majority spin band structure along the Γ to X (Z) direction. Here Δ_1 (a), Δ_5 (b), and Δ_2 (c) represent the (s, p_z, d_{z^2}), (p_x, p_y, d_{xz}, d_{yz}), and (d_{xy}, $d_{x^2-y^2}$) orbital characters, respectively.

this study, we first investigated the electronic structure properties of various Co_2MnSb surface terminations. We generated three types of surfaces by simulating the cleavage of the optimized bulk structure along the (001) crystal orientation: naturally terminating surfaces with Co-Co and Mn-Sb terminations, and an off-stoichiometric surface with a Mn-rich (Mn-Mn) termination obtained by replacing one of the surface Sb atoms with a Mn atom. To determine the relative stability of the different surfaces, we calculated their surface free energies and summarized the results in Table S3. Our results indicate that the Co-Co terminated surface has the lowest surface energy. However, the other two surface terminations exhibit negative surface energy, suggesting the possibility that they can be synthesized under non-equilibrium conditions, even though the Co-Co terminated surface may be easier to form.

To identify the surface with the highest SP, the electronic structure of various surfaces has been investigated, as shown in Figure S8. The results reveal that the Mn-Sb and Mn-Mn interfaces preserve the half-metallic (HM) property of the bulk, while the Co-Co surface destroys the HM character. The stronger localization of the *d*-electrons as compared to bulk, can be seen in S8, which leads to the increase in magnetic moments of the surface atoms, as shown in Table S3. Moreover, an increase in the exchange splitting energy for the surface atoms compared to the bulk is observed in Figure S8, resulting in larger surface magnetic moments.

The Mn-Sb and Mn-Mn terminated surfaces were found to possess high surface SP and thus, we further investigated their electronic and spin transport properties in conjunction with HfIrSb. In contrast, the Co-Co

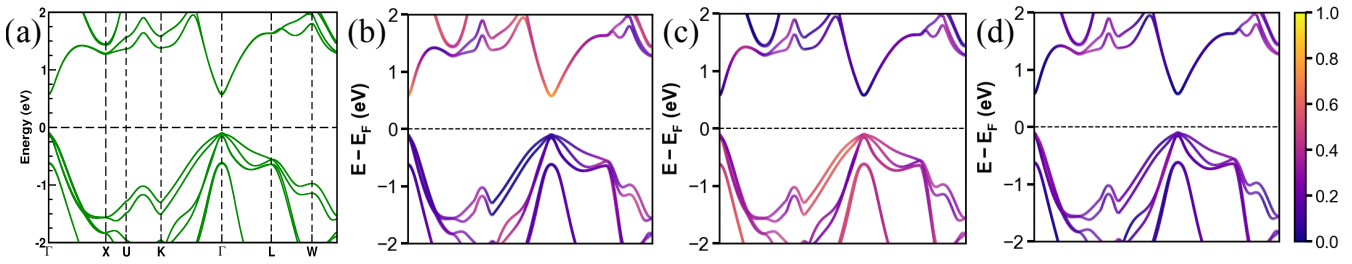

Figure S6. (a) The electronic band structure of HfIrSb, considering the influence of spin-orbit coupling interaction, is presented. Subsequent panels, (b), (c), and (d), illustrate the band structures resolved by orbital characteristics. Specifically, (b) represents (s, p_z, d_{z^2}) orbitals, (c) showcases (p_x, p_y, d_{xz}, d_{yz}) orbitals, while (d) displays (d_{xy}, $d_{x^2-y^2}$) orbital contributions, respectively.

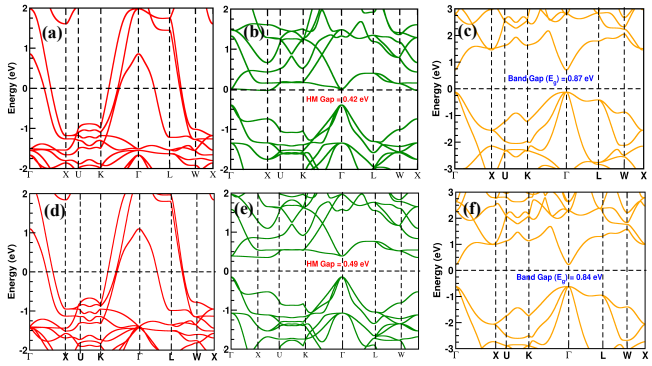

Figure S7. The electronic band structure of bulk Co2MnSb and HfIrSb computed using two different codes: the upper (lower) panel displays results obtained using VASP (QE). In these panels, (a), (d) and (b), (e) present the majority and minority spin bands of Co2MnSb, respectively. (c) and (f) give the band structure for HfIrSb.

interface was neglected as it showed relatively poor surface SP.

IV. ELECTRONIC DENSITY OF STATES & BAND STRUCTURE OF THE HETEROJUNCTION

To investigate the influence of interfacial interactions on electronic behavior, we analyze the projected DOS of the interface atoms, as depicted in Fig.S9. The atom projected DOS of the interfacial Mn atoms for both the Mn-Sb/Ir and Mn-Mn/Ir interfaces are shown in Fig.4 (a) and (d), respectively. Our analysis reveals that the half-metallic character of the bulk is disrupted for both interfaces. However, the Mn-Sb/Ir interface still exhibits a high degree of spin polarization (approximately 68%). The DOS of the different interface Mn atoms for the Mn-Mn/Ir interface significantly differ from each other. Specifically, the Mn_1 atom displays high majority spin density at around -1 eV, while the Mn_2 atom exhibits a slightly shifted density of states, which is towards the higher binding energy side (approximately -1.8 eV). This results in a higher exchange splitting energy and thus larger magnetic moment for the Mn_2 atom is observed.

We show various *d*-orbital contributions of the Mn atom for the Mn-Sb/Ir and Mn-Mn/Ir interfaces in Fig.S9 (c) and (f), respectively. Here, d_1, d_2, d_3 correspond to the d_{z^2}, (d_{xy}, $d_{x^2-y^2}$), and (d_{yz}, d_{xz}) orbitals of the interface Mn atoms, respectively. Though the formation of the heterojunction breaks the periodicity along the z-direction, the d_1 orbital retains the half-metallic character of the bulk. However, the d_2 and d_5 orbitals are primarily responsible for the destruction of the half-metallicity at the interface. There is a significant difference between the majority spin DOS at the E_F for the two interfaces. For the Mn-Sb/Ir interface, there is a dominant contribution from the d_5 orbitals (Fig.S9 (c)), while for the Mn-Mn/Ir interface, both d_2 and d_5 orbitals have a significant contribution. Since the orbital characters of the traveling electrons play a crucial role in transmission, one would expect differences in the spin-transmission behavior between these two interfaces, which are discussed in the subsequent section.

The Ir atom at the interface becomes metallic for both interfaces, while the semiconducting behaviors persist in the bulk region (Fig.S9 (b), (e)). Consequently, there is a small gain in magnetic moments (approximately -0.1 μ_B) for the interface Ir atoms for both interfaces.

Figure.S12 shows a comparison of total DOS of the interface atoms for each interfaces of Co_2MnSb/HfIrSb heterojunction, with considering the effect of SOC and without SOC. As depicted in Figure.S12 , the DOS around the E_F gets hardly affected by SOC. Therefor we do not include the effect of SOC for the transmission calculation.

To achieve a high TMR ratio, it is essential to minimize the current passing through the barrier when the magnetization of the electrodes is anti-parallel. When perfect half-metallic electrodes are used, spin flipping and tun-

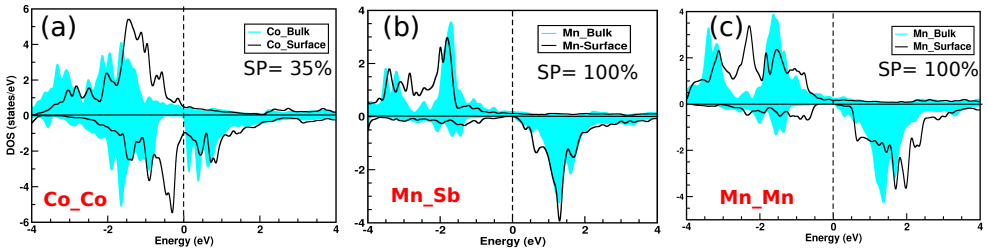

Figure S8. Atom projected density of states and respective values of spin polarization for different surface terminations along the (001) crystal orientation of Co_2MnSb.

Table S3. The surface free energy (σ_F in eV/Å^2), spin-polarization (SP in %) and magnetic moments (in μ_B) the surface atoms (Mn atom for Mn-Sb and Mn-Mn termination and Co atom for Co-Co termination) of various terminations of Co_2MnSb along (001) crystal orientations. The magnetic moments of the atoms inside the bulk are mentioned inside the bracket.

Surface termination	σ_F	Magnetic moment	SP
Mn-Sb	-4.1267	3.81 (3.46)	100
Co-Co	-4.1885	1.19 (1.31)	35
Mn-Mn	-4.0271	3.81, 3.85 (3.45)	100

Table S4. Net charge transfer at the interface (in e), from Bader[9] analysis based on the VASP and Mulliken and Loewdin charge as obtained from LOBSTER package[10].

Surface termination	Interface atom	Bader	Mulliken	Loewdin charge
Mn-Sb	Mn	-0.14	-0.11	-0.08
	Sb	-0.08	-0.24	-0.15
	Ir	-0.27	-0.19	-0.12
Mn-Mn	Mn_1	-0.03	-0.07	-0.06
	Mn_2	-0.06	-.06	-0.04
	Ir	-0.29	-0.43	-0.33

neling to or from an interfacial state can produce current in an anti-parallel configuration. The tunneling probability of carriers in various bands can vary significantly depending on their band symmetry, as demonstrated in the literature.[1,11] Electrons in states with Δ_1 orbital symmetry exhibit weak decay within the barrier material, whereas the transmission of electrons in other symmetry states is exponentially suppressed. Our prior research[12] illustrated the presence of Δ_1 symmetric bands in the majority spin channel for Co_2MnSb. This suggests that it is easy for majority spin electrons to tunnel through the barrier in a parallel spin configuration, which is a prerequisite for achieving a high TMR.

Nonetheless, it is equally important to reduce the tunneling rate into minority interface states to suppress the current for anti-parallel magnetization. We present the band structure of minority spin states for the heterojunction with Mn-Sb/Ir and Mn-Mn/Ir interfaces in Fig.S10. In Fig.S10(b) and (e), we demonstrate the contribution of interface atoms (i.e., Mn, Sb, and Ir) to the minority spin bands. The orbital projected band structures of the interface atoms in Fig. 5(c) imply that the minority spin conduction bands for the Mn-Sb/Ir interface have a dominant Δ_1 character, suggesting a larger transmission for the minority states. Conversely, for the Mn-Mn/Ir interface Fig.S10(f), mostly in-plane d orbitals dominate the minority spin states near E_F, leading to poor coupling with the Δ_1 type bands of the HfIrSb spacer material.

Bader Charge and COHP Bond Analysis: The net charge transfer at Co_2MnSb/HfIrSb interfaces as calculated from Bader charge analysis[13] is shown in Fig. S10[14]. For both the interfaces we observe that the Ir atom at the interface loses significant amount of charge (-0.27e) compared to the interface Mn (-0.14e) and Sb (-0.07e) atom, that get accumulated in the interface region. Similar trend can also be observed from our Mulliken and Loewdin charge analysis (Table S4.[14]) as obtained from LOBSTER package[10]. Additionally, our orbital-decomposed charge density analysis, facilitated by the LOBSTER package[10], highlights that out-of-plane orbitals (s and d_{z^2} for Ir and p_z for Sb) witness the most significant charge losses, whereas for Mn, it

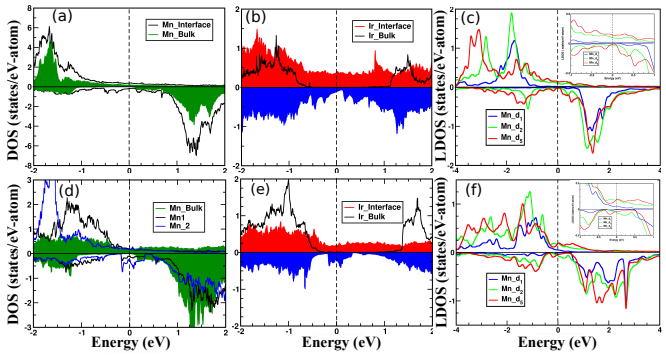

Figure S9. The local density of states (LDOS) for the interfacial Mn, and Ir atoms are shown in panels ((a), (b)), and ((d), (e)), respectively, for the heterojunctions with Mn-Sb/Ir (top panel) and Mn-Mn/Ir (bottom panel) interfaces. The LDOSs in the bulk region are also presented as a reference using filled curves in each figure. Panels (c) and (f) display the orbital projected DOS of the interfacial Mn atom for the heterojunctions with Mn-Sb/Ir and Mn-Mn/Ir interfaces, respectively, with d_1, d_2, d_3 denoting d_{z^2}, (d_{xy}, $d_{x^2-y^2}$), and (d_{yz} d_{xz}) orbitals, respectively.

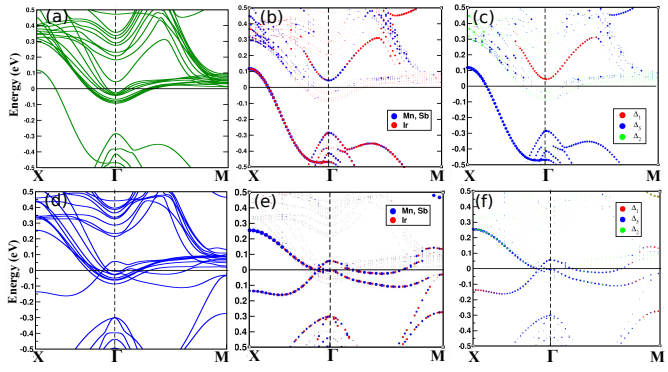

Figure S10. (a) & (d) Minority spin band structure for the considered heterojunctions with Mn-Sb/Ir & Mn-Mn/Ir interface on the top (bottom) panel along the X-Γ-M high symmetry directions of the 2D Brillouin zone; (b), (c) [(e), (f)] represent the atomic and orbital contribution of the inter-facial atoms on the minority spin band structures for Mn-Sb/Ir [Mn-Mn/Ir] interface, respectively. Here Δ_1 Δ_2 and Δ_5 represent (s, p_z, d_{z^2}) , (d_{xy}, $d_{x^2-y^2}$), and (p_x, p_y, d_{yz} d_{xz}) orbitals respectively.

is the in-plane ($d_{x^2-y^2}$, d_{xz}) orbital that experiences substantial charge loss. These findings corroborates well with our charge density and magnetization density difference analysis presented in Fig.3.

To gain deeper insights into the interface bonding, we conducted the COHP analysis between Mn-Ir and Sb-Ir atom pairs, as depicted in Fig. S13. The Crystal Orbital Hamilton Population (COHP) analysis has

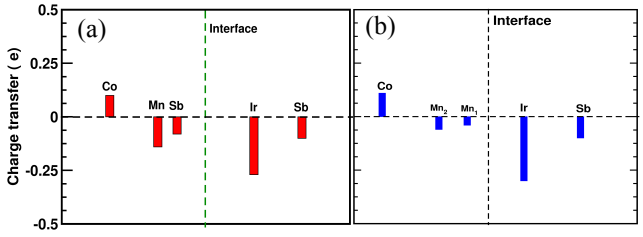

Figure S11. Charge transfer at the Co_2MnSb/HfIrSb interface as calculated from the Bader analysis: (a), (b) for Mn-Sb/Ir and Mn-Mn/Ir interface, respectively.

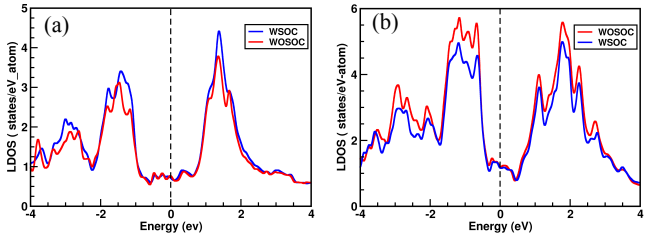

Figure S12. Comparison of total density of states of the interface atoms with and without considering the effects of spin-orbit-coupling for: (a) Mn-Sb/Ir , (b)Mn-Mn/Ir interface, respectively.

been carried out using the LOBSTER package[10,15].The pbeVaspFit2015 basis with the following basis functions: Co: 3d, 4s, and 3p; Mn: 4s, 3d and 4p; Sb: 5s, 4d and 5p; Hf: 5d, 6s and 5p ; Ir: 5d, 6s and 4f, have been used for the orbital projection of plane waves. The wavefunctions are obtained from the DFT calculations. Additionally, in Fig. S13, we present integrated COHP values (ICOHP) between these atom pairs, serving as an indicator of bond strength by integrating the COHP values up to the (E_F). For the Mn-Sb/Ir interface (Fig. S13 (a)), the COHP analysis between Mn-Ir atom reveals presence of anti-bonding states near E_F in the majority spin channels, which lowers the bonding interaction. However, the situation is different for the minority-spin channel, where the whole valence band (VB) has bonding interaction. Similar observations have also been made in some previous bonding analysis involving $3d$ transition metal atoms[16–18]. Because, of the exchange hole, the majority spin orbitals are more spatially contracted than the minority spin orbitals and contributes less to the bonding interactions[16]. The COHP bonding analysis between the Ir-Sb pair mostly revealed bonding interaction in the valence band for both the spin channel, apart from the presence of small anti-bonding interaction in the minority spin-channel in the VB away from E_F, which is compensated by the strong bonding character deep into the energy. The ICOHP values in Fig. S13 indicates the Sb-Ir (ICOHP:-2.35 eV) bonding is significantly stronger

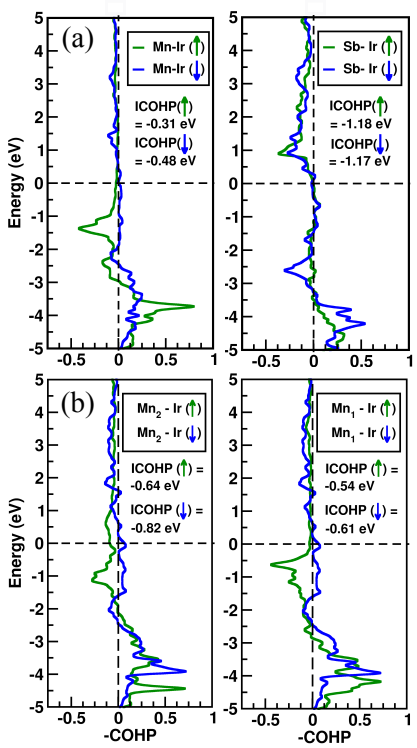

Figure S13. COHP analysis of the bonds between the interface atoms for Co_2MnSb/HfIrSb heterojunction: (a) Mn-Sb/Ir ; (b) Mn-Mn/Ir interface, respectively. E_F has been set to 0 eV. The positive (negative) values at the x-axis indicates bonding (anti-bonding) feature. The sign ↑(↓) indicate majority (minority) spin contributing to the bonding.

than the Mn-Ir (ICOHP:-0.79 eV) bonding at the interface.

In the case of the Mn-Mn/Ir interface, the COHP analysis uncovers anti-bonding states in the majority spin channels near E_F between the both, Mn_1-Ir and Mn_2-Ir bonds, contributing to even weaker bonding compared to the Mn-Sb/Ir interface. In contrast, the minority-spin contributes exclusively to the bonding interaction below E_F (Fig. S13 (b)).

The weaker covalent bonding at the Mn-Mn/Ir interface compared to the Mn-Sb/Ir interface, as indicated by our COHP bonding analysis is further supported by the Bader charge analysis, which suggests relatively less charge transfer at the Mn-Mn/Ir interface compared to the Mn-Sb/Ir Interface (Fig. **??**). For the Mn-Sb/Ir interface, the COHP analysis reveals predominantly positive values at deeper energy values from E_F between Mn-Ir and Sb-Ir atoms, indicating a bonding feature. However, a notable anti-bonding feature also emerges below E_F, approximately at -1.5 eV, for Mn-Ir, which weakens the Mn-Ir bonding compared to the Sb-Ir bonding at the interface. This weakening is further evident in the calculated ICOHP values shown in Fig.S13 (a).In the case of the Mn-Mn/Ir interface, the COHP analysis uncovers anti-bonding states near E_F between Mn_1-Ir and Mn_2-Ir bonds, contributing to even weaker bonding compared to the Mn-Sb/Ir interface. This observation is further supported by the Bader charge analysis, which indicates relatively less charge transfer at the Mn-Mn/Ir interface compared to the Mn-Sb/Ir Interface.

V. ELECTRONIC PROPERTIES OF THE HETEROJUNCTION & BULK SPACER LAYER UNDER BI-AXIAL STRAIN

In order to investigate the underlying mechanism of such orbital sensitive majority transmission, we have conducted a detailed analysis of the electronic properties of the bulk electrode and spacer material. Our previous discussion has revealed that bi-axial strain induces changes in the spin polarization of the electrode, resulting in the loss of its HM property under compressive bi-axial strain (as shown in Fig. S2[14]). However, we have not observed any significant changes in the orbital character of the bands under the entire range of applied strain along the transport direction (Γ to X (Z)), as depicted in Figures S3, S4[14]. Somewhat rigid shift of the bands can only be seen.

Additionally, we have demonstrated the effect of bi-axial strain on the electronic properties of the bulk spacer material HfIrSb, as illustrated in Fig. S14. Specifically, under -4% bi-axial strain, HfIrSb becomes an indirect bandgap semiconductor, with an increase in the bandgap of 1.25 eV compared to the unstained structure, and the degeneracy of the valence bands at the Γ point is also lifted. Furthermore, the atom-projected band structure analysis suggests that both the VBM at Γ and CBM at the M point have a dominant contribution from the Hf atoms (as shown in Fig. S14(a)), which is unlike the case of the unstained structure (as shown in Fig.1). These changes are also reflected in the orbital-projected band structure (as presented in Fig. S14 (a)), where we observe that the VBM and CBM have Δ_2 and Δ_5 orbital characters, respectively.

On the other hand, under +4% bi-axial strain, we observe that the CBM is mostly Sb atom derived and the VBM has a contribution from both Hf and Ir atoms (as illustrated in Fig. S14(b)). The orbital-projected band structure shows, the VBM is mostly dominated by the Δ_5 orbitals. The comprehensive differences in the electronic properties of the spacer layer under compressive and tensile bi-axial strain lead to the orbital sensitivity of the majority spin transmission. Finally, we analyze the results corresponding to the d orbitals of the interfacial Mn atoms of the heterojunction with Mn-Mn/Ir interface under -4% (compressive) and +4% (tensile) strain (Fig.S15). Our results clearly indicate that under -4% strain, the $d_{x^2-y^2,xy}$ orbitals of the Mn atoms have a significant contribution to the majority spin states at the Fermi level, whereas it is the $d_{xz,yz}$ orbitals of Mn atom that contributes more for +4% strain. These ob-

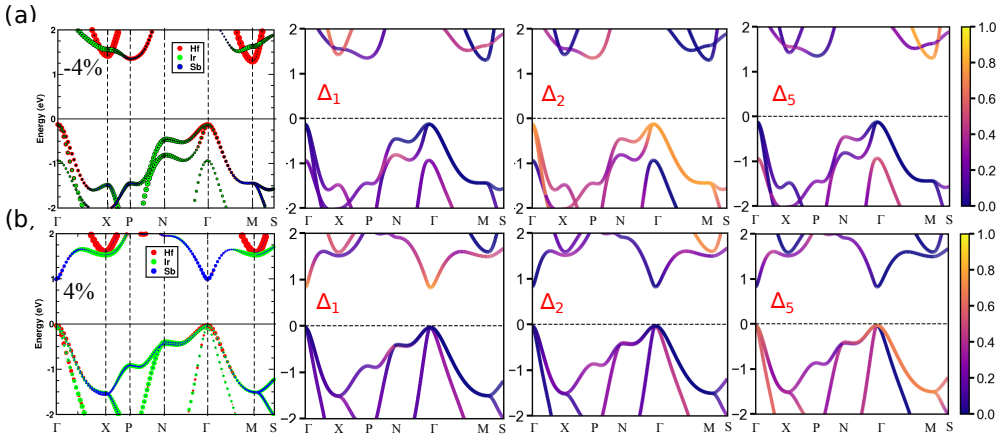

Figure S14. The atom and orbital projected band structure of bulk HfIrSb under strain is investigated, specifically for (a) -4% (compressive) strain and (b) +4% (tensile) strain. In this analysis, the symbols Δ_1, Δ_2, and Δ_5 represent the following orbital compositions, respectively: (s, p_z, d_{z^2}), (d_{xy}, $d_{x^2-y^2}$), and (p_x, p_y, d_{yz}, d_{xz}).

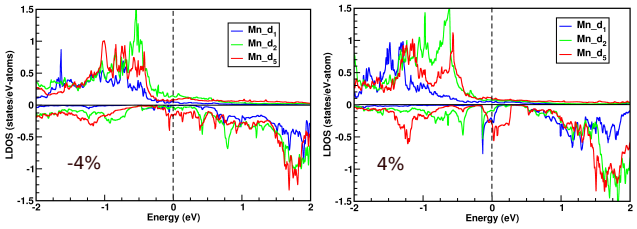

Figure S15. Orbital projected DOS of interfacial Mn atom under 4% compressive and tensile strain for Mn-Mn/Ir interface.Here, d_1, d_5, d_2 represents d_{z^2}, $d_{xz,yz}$, *and* $d_{x^2-y^2,xy}$ orbitals , respectively.

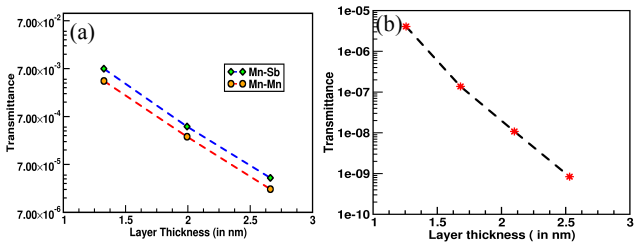

Figure S16. Transmittance in parallel spin configurations with varying spacer layer thickness: (a) & (b) with HfIrSb and MgO spacer, respectively.

servations collectively explain the orbital sensitivity of the majority spin transmission under strain.

VI. SPIN TRANSMISSION PROPERTIES OF THE HETEROJUNCTION

VI.1. Transmittance in Parallel Spin Configurations with Spacer Layer Thickness:

Within Figure S16, we undertook a comparison of the transmittance characteristics between HfIrSb and MgO in a parallel spin configuration, utilizing various layer thicknesses. As anticipated, owing to the larger band gap of MgO, the transmittance value is observed to be 1000 times smaller, even with comparable barrier thickness. This observation alludes to a notably elevated RA-product for MgO in contrast to HfIrSb.

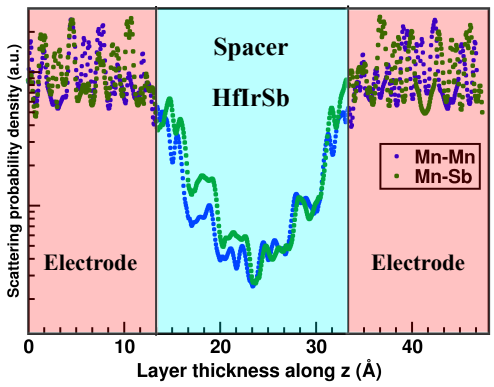

Figure S17. The absolute square of the right propagating scattering state wavefunctions at the Fermi energy (E_F) within the Co_2MnSb/HfIrSb heterojunction (with 13ML of spacer) is depicted. The illustration showcases the penetration and decay of the wavefunction for two different interfaces, Mn-Sb/Ir and Mn-Mn/Ir, as a function of layer thickness.

[1] Miura, Y.; Uchida, H.; Oba, Y.; Abe, K.; Shirai, M. Half-metallic interface and coherent tunneling in Co_2YZ/MgO/Co_2YZ (YZ = MnSi, CrAl) magnetic tunnel junctions: A first-principles study. *Phys. Rev. B* **2008**, *78*, 064416.

[2] Guillemard, C.; Petit-Watelot, S.; Pasquier, L.; Pierre, D.; Ghanbaja, J.; Rojas-Sánchez, J.-C.; Bataille, A.; Rault, J.; Le Fèvre, P.; Bertran, F.; Andrieu, S. Ultralow Magnetic Damping in Co_2Mn-Based Heusler Compounds: Promising Materials for Spintronics. *Phys. Rev. Applied* **2019**, *11*, 064009.

[3] Enamullah,; Lee, S.-C. High-efficient and defect tolerant Co2MnSb ternary Heusler alloy for spintronic application. *Journal of Alloys and Compounds* **2018**, *765*, 1055–1060.

[4] Gautier, R.; Zhang, X.; Hu, L.; Yu, L.; Lin, Y.; Sunde, T. O. L.; Chon, D.; Poeppelmeier, K. R.; Zunger, A. Prediction and accelerated laboratory discovery of previously unknown 18-electron ABX compounds. *Nature Chemistry* **2015**, *7*, 308–316.

[5] Arikan, N.; DikiCi Yildiz, G.; Yildiz, Y. G.; İyigör, A. Electronic, Elastic, Vibrational and Thermodynamic Properties of HfIrX (X = As, Sb and Bi) Compounds: Insights from DFT-Based Computer Simulation. *Journal of Electronic Materials* **2020**, *49*, 3052–3062.

[6] Lee, M.-S.; Poudeu, F. P.; Mahanti, S. D. Publisher's Note: Electronic structure and thermoelectric properties of Sb-based semiconducting half-Heusler compounds [Phys. Rev. B 83, 085204 (2011)]. *Phys. Rev. B* **2011**, *83*, 159907.

[7] Kresse, G.; Furthmüller, J. Efficient iterative schemes for ab initio total-energy calculations using a plane-wave basis set. *Phys. Rev. B* **1996**, *54*, 11169–11186.

[8] Baroni, S.; de Gironcoli, S.; Dal Corso, A.; Giannozzi, P. Phonons and related crystal properties from density-functional perturbation theory. *Rev. Mod. Phys.* **2001**, *73*, 515–562.

[9] Bader, R. A Quantum Theory. **1990**,

[10] Dronskowski, R.; Bloechl, P. E. Crystal orbital Hamilton populations (COHP): energy-resolved visualization of chemical bonding in solids based on density-functional calculations. *The Journal of Physical Chemistry* **1993**, *97*, 8617–8624.

[11] Hülsen, B.; Scheffler, M.; Kratzer, P. Structural Stability and Magnetic and Electronic Properties of Co_2MnSi(001)/MgO Heterostructures: A Density-Functional Theory Study. *Phys. Rev. Lett.* **2009**, *103*, 046802.

[12] Bhattacharya, J.; Chakrabarti, A. Electronic and transport properties of Heusler alloy based magnetic tunneling junctions: A first principles study. *Computational Materials Science* **2023**, *216*, 111852.

[13] Henkelman, G.; Arnaldsson, A.; Jnsson, H. A fast and robust algorithm for Bader decomposition of charge density. *Computational Materials Science* **2006**, *36*, 354–360.

[14] Bhattacharya, J.; Rawat, A.; Pati, R.; Chakrabarti, A.; Pandey, R. Supporting Information. **2023**,

[15] Deringer, V. L.; Tchougréeff, A. L.; Dronskowski, R. Crystal Orbital Hamilton Population (COHP) Analysis As Projected from Plane-Wave Basis Sets. *The Journal of Physical Chemistry A* **2011**, *115*, 5461–5466.

[16] Nelson, R.; Konze, P. M.; Dronskowski, R. First-Principles Chemical Bonding Study of Manganese Carbodiimide, Mn-NCN, As Compared to Manganese Oxide, MnO. *The Journal of Physical Chemistry A* **2017**, *121*, 7778–7786.

[17] Landrum, G. A.; Dronskowski, R. The Orbital Origins of Magnetism: From Atoms to Molecules to Ferromagnetic Alloys. *Angewandte Chemie International Edition* **2000**, *39*, 1560–1585.

[18] Bhattacharya, J.; Pandey, D.; Barman, S. R.; Chakrabarti, A. Surface termination and thickness dependent magnetic coupling of Cr adlayers on Ni2MnGa(001) surfaces: An ab initio study. *Journal of Magnetism and Magnetic Materials* **2021**, *540*, 168398.